Article

Direct Measurement of Interhelical DNA Repulsion and Attraction by Quantitative Cross-Linking

Ian Hamilton, Magdalena Gebala, Daniel Herschlag, and Rick Russell*

Cite This: https://doi.org/10.1021/jacs.1c11122

Read Online

ACCESS | 📊 Metrics & More | 📖 Article Recommendations | 🆘 Supporting Information

ABSTRACT: To better understand the forces that mediate nucleic acid compaction in biology, we developed the disulfide cross-linking approach xHEED (X-linking of Helices to measure Electrostatic Effects at Distance) to measure the distance-dependent encounter frequency of two DNA helices in solution. Using xHEED, we determined the distance that the electrostatic potential extends from DNA helices, the dependence of this distance on ionic conditions, and the magnitude of repulsion when two helices approach one another. Across all conditions tested, the potential falls to that of the bulk solution within 15 Å of the major groove surface. For separations of ~30 Å, we measured a repulsion of 1.8 kcal/mol in low monovalent ion concentration (30 mM Na^+), with higher Na^+ concentrations ameliorating this repulsion, and 2 M Na^+ or 100 mM Mg^{2+} eliminating it. Strikingly, we found full screening at very low Co^{3+} concentrations and net attraction at higher concentrations, without the higher-order DNA condensation that typically complicates studies of helical attraction. Our measurements define the relevant distances for electrostatic interactions of nucleic-acid helices in biology and introduce a new method to propel further understanding of how these forces impact biological processes.
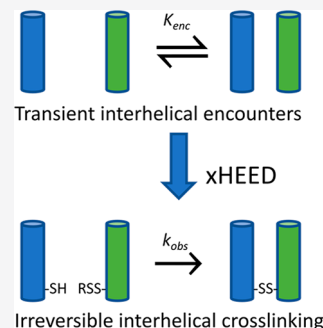
INTRODUCTION

Nucleic acid compaction is an essential feature of key biological processes including chromatin condensation,[1−4] viral packaging,[5,6] and the formation of structured RNAs.[7−14] In all of these processes, DNA or RNA helices come into close proximity or physical contact with other helical segments. Owing to the high negative charge density of the phosphodiester backbone, the approach of nucleic acid helices to one another is strongly disfavored by mutual electrostatic repulsion.[15] Thus, in processes requiring compaction, this electrostatic repulsion must be overcome by counterions, proteins, and/or direct nucleic acid contacts such as the tertiary contacts found in functional RNAs.

To understand nucleic acid compaction, a key challenge is to determine the magnitude and spatial distribution of the electrostatic repulsion between helical segments and the factors that create and modulate it. Nucleic acids carry with them an ion atmosphere, a dynamic sheath of loosely associated ions that is enriched with cations, depleted of anions, and has a net charge that neutralizes the negative charges on the nucleic acid backbone. The ion atmosphere mitigates or "screens" the electrostatic potential arising from these negative charges, decreasing its magnitude with increased distance from the helix until it is reduced to background levels.[7,16−19] Nucleic acid compaction necessitates a close proximity of helices to each other, potentially to distances with very large electrostatic potential despite mitigation by the ion atmospheres.[15,20] Thus, the size and spatial distribution of the electrostatic potential, which depend strongly on ion concentrations, have profound impacts on the interactions of nucleic acids with other helices, as well as interactions with proteins and other molecules required for biological function.[1,2,20−25] We have extensive experimental information on the composition of the ion atmosphere that surrounds nucleic acids,[2,8,11,19,26−30] but not the size and spatial distribution of the electrostatic potential that governs their interactions and thus determines the strategies needed by biology to manipulate and control DNA and RNA in cells.

With the challenges of experimental studies for measuring the electrostatic potential and its spatial distribution, considerable effort has been directed to developing models of nucleic acid electrostatics. The Poisson−Boltzmann (PB) formalism provides a generalized view and is widely used to model the electrostatic potential near nucleic acids and other macromolecules,[9,15,19,31,32] including aspects of nucleic acid compaction.[2,14,33] Its modest computational demands and demonstrated predictive utility in certain instances[9,19,31−33] have secured its place as the most commonly used modeling technique. Nevertheless, the mean-field treatment of ions and solvent in PB modeling ignores effects stemming from the size, solvation, and correlated behavior of individual ions.[28,33−38] Modified or alternative models have been successful in matching some experimental parameters but likely lack the atomic-level
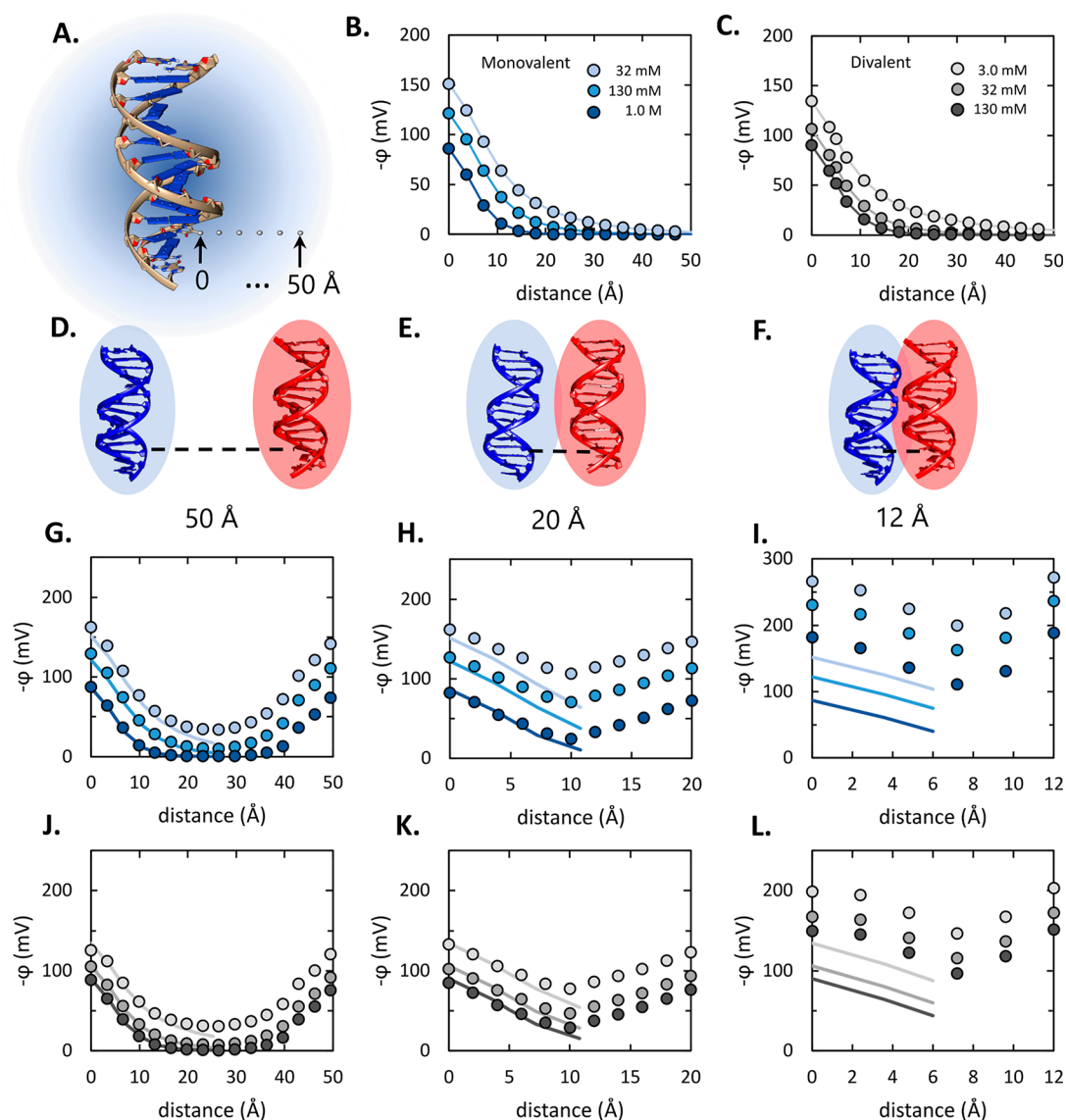
Figure 1. Poisson−Boltzmann (PB) predictions of the electrostatic potential (φ) generated by DNA helices and electrostatic screening. (A) Schematic of the electrostatic potential surrounding an isolated dsDNA. The potential decreases with increasing distance from the DNA, as shown by the color gradient, due to screening from the ion atmosphere. Distances here and elsewhere are measured from C5 of a thymidine residue, within the major groove. (B,C) PB calculations of electrostatic potential along the path marked by spheres in panel A with (B) monovalent and (C) divalent ions at various concentrations. (D−F) Schematics of two DNA helices separated by 50, 20, and 12 Å. (G−I) PB calculations of electrostatic potential between two helices along coordinates indicated by dashed lines in panels D−F, respectively (i.e., for distances of 50, 20, and 12 Å). Colors represent monovalent ion concentrations as in panel B. Dots are calculated potentials (in mV) between DNA helices, and solid curves are potentials calculated around a single dsDNA as shown in panel B. (J−L) PB calculations as in panels G−I, but with divalent ion concentrations, colored as in panel C. Calculations are shown for helices in a parallel orientation. Calculations performed with different orientations yielded similar local potentials across the gap of closest approach (Figure S13).

detail needed to robustly describe and predict electrostatic properties of nucleic acids.[34,38−43]

Here, we developed and applied an approach to quantitatively study the energetics of interactions between nucleic acid helices. Specifically, we adapted a method used previously to probe RNA folding[44,45] to develop xHEED (X-linking of Helices to measure Electrostatic Effects at Distance), a quantitative, distance-tunable disulfide cross-linking assay. We then used xHEED to measure the frequency of close encounters between 15-bp DNA helices under a range of solution conditions related to those found in biology. We observed repulsion at low concentrations of monovalent and divalent cations and showed that the potential extends 10−15 Å at low ionic strength (30 mM Na⁺)

and 10 Å at high ionic strength (2.5 M Na²⁺ or 50 mM Mg²⁺). PB modeling greatly overestimates the strength of the repulsion at low ion concentrations, underscoring the importance of atomic features of the ion atmosphere for nucleic acid energetics. We also detected and quantified a net pairwise attraction between DNA helices in the presence of the trivalent cation $Co(NH_3)_6^{3+}$, highlighting the potential of the xHEED method to provide new information on the forces that impact nucleic acid compaction in nature.

Background. Poisson−Boltzmann calculations provide a framework for understanding the electrostatic consequences of bringing two nucleic acid helices close to each other.[46,47] PB predicts that an electrostatic potential around an isolated DNA
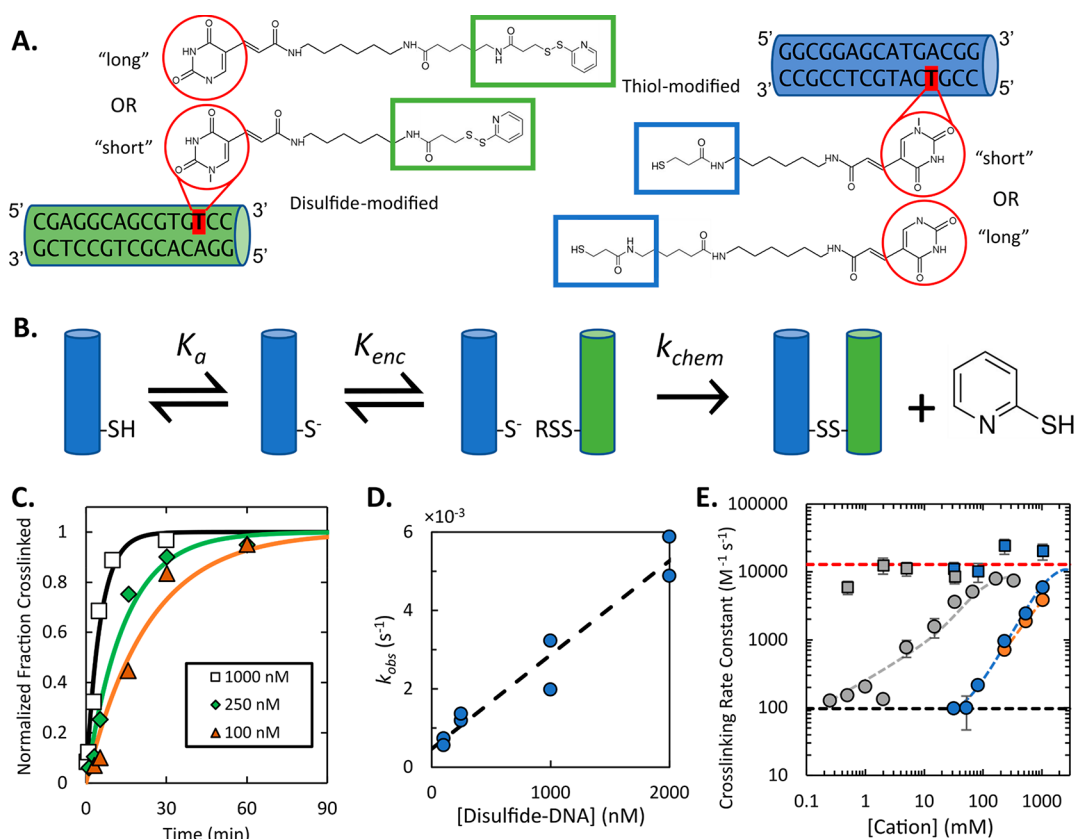
Figure 2. Disulfide cross-linking method (xHEED) and reactions. (A) DNA helix constructs. Modified thymidine residues (highlighted red) are attached at C5 to either a terminal thiol or a pyridyl disulfide by linkers extending ~10 Å ("short", Figure S1A) or ~20 Å ("long", Figure S1B). (B) Schematic of interhelical disulfide cross-linking. The reaction comprises three steps: thiol deprotonation (K_a), helix encounter (K_{enc}), and disulfide exchange (k_{chem}). The first two steps occur in either order and are in the order shown because $K_a \gg K_{enc}$ under our experimental conditions. (C) Representative cross-linking progress curves for single reactions, with the indicated concentrations of the disulfide helix and 530 mM Na⁺. Curves show the best fits by a pseudo-first-order rate equation. Cross-linking fraction is normalized by observed reaction end points, which typically ranged from 35 to 50% owing to a fraction of inactive thiol-modified oligonucleotides. (D) Plot of pseudo-first-order rate constant as a function of the disulfide-containing helix concentration. Each point is a rate constant measurement from a single reaction and the plot shows data from the reactions in panel C and additional reactions at the same solution conditions. (E) Observed second-order rate constants with Na⁺ (blue, 30−1000 mM), K⁺ (orange, 200−1000 mM), and Mg²⁺ (gray, 0.25−330 mM), probing interhelical separations of ≤20 Å (circles) and ≤40 Å (squares). All rate constants here were measured at pH 9.0 and were determined from linear fits of least three pseudo-first-order rate constant measurements. Error bars show regression standard error and are smaller than the marker in some cases. Dashed horizontal lines indicate the rate constant with buffer only (30 mM Na⁺, black, 97 $M^{-1}\ s^{-1}$) and the maximal rate constant with the uncharged 2-aldrithiol (red, $1.3 \times 10^4\ M^{-1}\ s^{-1}$). Dashed curves are guides only.

helix decreases exponentially with increasing distance from the helix and its size (the distance its influence extends into the bulk) depends on the salt concentration and valence in the process referred to as electrostatic screening (Figure 1A−C). Specifically, PB modeling predicts that the electrostatic potential decreases to essentially 0 mV at a distance of 40−50 Å in the presence of 30 mM monovalent salt, whereas at 1.0 M monovalent salt this distance is reduced to 15−20 Å (Figure 1B). (Here and below, distances are measured from the site of linker attachment in the cross-linking experiments, the C5 position of a thymidine residue in the major groove (Figure 2A), ~5 Å from the helical axis.) Divalent ions produce more potent screening than monovalent ions, with far lower concentrations required to shorten the decay distance (Figure 1C).

In biology, DNA and RNA helices form structures with interhelical distances that are expected to be disfavored by the negative electrostatic fields surrounding each helix.[47] The degree to which helical approach is disfavored can be evaluated in terms of the combined electrostatic potential generated by the two helices. A way to think about this effect is that work is required to create or strengthen a potential, so the increased strength of this

potential reflects the work required to bring the helices together to a particular distance.[48] Because the electrostatic potential extends to a greater distance at low ionic strength than high ionic strength, and likewise with monovalent cations than with multivalent cations at a given concentration (Figure 1B,C), the repulsion between helices is predicted to extend to larger interhelical separations under low-salt-concentration and low-valence-ion conditions.

To explore the predicted behavior and to guide our experimental design, we used PB to calculate electrostatic potentials between two DNA helices at separations of 50, 20, and 12 Å in the presence of various concentrations of monovalent and divalent cations, and we compared these potentials to those generated by the isolated DNA helices (Figure 1D−I). With an interhelical separation of 50 Å, PB predicts that the electrostatic potentials are essentially unaffected by the presence of the other helix, deviating little from that of an isolated helix and decreasing nearly to zero at a position equidistant from the two helices, even at the low ionic strength of 30 mM monovalent salt (Figure 1D,G; dots vs lines in Figure 1G). Thus, the helices would be expected to approach

each other to this distance with the same frequency as if one or both of the helices were electrically neutral.

When the DNA helices are moved closer together, e.g., to a separation of 20 Å, at the low ionic strength of 30 mM monovalent salt, the regions of potential from each helix calculated by PB extend beyond the midpoint between the two helices (Figure 1E,H). As a result, the electrostatic potential of each helix is increased by the approach of the other helix, producing a mutual repulsion. In contrast, at 1 M Na$^+$, the electrostatic potential is predicted to drop nearly to the background level between the two helices (10 Å from each helix). With an even smaller separation of 12 Å (Figure 1F,I), the electrostatic potential between the DNA helices is increased to a value approximately 100 mV (4 kT/e or 2.5 kcal mol^{-1} e^{-1}) higher at the midpoint than the potential generated by the single DNA helix at the same distance from the helix.

An analogous picture emerges with divalent cations, but with substantially lower ion concentrations required to transition between the regimes with and without repulsion between the two helices (Figure 1J−L). Comparable effects are predicted with an order of magnitude lower concentrations of divalent cations than monovalent cations. Additionally, divalent cations are predicted to provide screening to closer separations between helices than monovalent cations, with a consequent shallower dependence of the interhelical repulsion on separation (e.g., compare Figure 1 panels I and L).

The Disulfide Cross-Linking Approach (xHEED). The xHEED approach measures the energetics of repulsion or attraction when two helices approach each other to within a defined distance. The central idea is that the second-order rate constant for cross-linking reports on the frequency of helical approach to a distance dictated by the combined lengths of the linkers holding the cross-linking probes. Critically, this rate constant is benchmarked against the corresponding rate constant for an equivalent reaction in which one of the DNA helices is replaced by a neutral small molecule with a chemically equivalent cross-linker. This comparison, along with additional controls described below (see Results), allows us to isolate and measure the energetic effect of the electrostatic potentials that surround the helices.

In the system used here, a single thymidine residue on each helix is modified with a linker, one with a thiol and the other with a disulfide (Figures 2A, S1). The deprotonated thiolate acts as a strong nucleophile to link the two helices by a disulfide bond (Figure 2B). The thiolated helix is radiolabeled, enabling determination of the fraction of cross-linked product with a native polyacrylamide gel (Figure S1C).

The cross-linking probes are attached to 15-bp DNA helices through linkers of 14 or 21 covalent bonds from the C5 position of thymidine residues (abbreviated "short" and "long" linkers, respectively; Figure 2A). These linkers are not expected to impact the behavior of the ion atmosphere, as they are uncharged, and the ordering of water in the vicinity of small hydrophobic solutes is not expected to differ substantially from the bulk.[49−51] Unless otherwise indicated, all distances are defined relative to this attachment point, which is within the major groove and ~5 Å from the helical axis. To estimate the lengths of the linkers, we modeled their behavior by a simple self-avoiding walk (SAW), combined with PB calculations to account for effects of the negatively charged thiolate ion (see Supporting Information, *Estimation of Average Linker Extensions* and Figure S2). This analysis suggested that the linkers extend on average ~10 Å (short) or ~20 Å (long) from their

attachment points, enabling the capture of encounters at helix−helix separations of up to ~20 Å or up to ~40 Å by using short or long linkers, respectively (Figures 2A, S1A,B). We also probed intermediate distances, for separations of up to ~30 Å, by using one short linker and one long linker. Linkers were attached 3 or 4 bp from the end of each helix (Figure 2A), and reactions with linkers attached at the central base pair of each helix (position 8) gave similar results (Figure S3).

In addition to measuring the energetics of helical approach under a defined set of conditions, we used the method to determine how ion concentration, ion identity, and distance from the helix impact these energetics. Thus, we varied the ion concentration and identity, while varying the separation distance that the two helices would need to attain for cross-linking via the linker lengths of cross-linking probes.

We also measured the energetics of helical approach in the presence of the trivalent ion cobalt hexamine $(Co(NH_3)_6^{3+})$. Previous studies have shown that DNA can undergo condensation transitions in the presence of this multivalent cation,[52−55] but the higher-order nature of this process has prevented detailed quantitative analysis, and PB is not applicable because, as a mean-field theory without explicit atoms, it can only predict the amelioration of repulsive interactions between negatively charged nucleic acids and not attractive forces that require atomic-level properties. Because DNA condensation is observed in the presence of biologically relevant polyamines with valence >2,[56−60] there is considerable interest from a biological perspective in understanding the magnitude and origin of attractive forces. An analogous condensation transition was suggested as a possible explanation for Mg^{2+}-induced collapse of structured RNAs.[61,62] Although subsequent studies showed that Mg^{2+} does not induce significant net pairwise attraction between helices,[20,33] we still lack quantitative experimental measures of the effects of Mg^{2+} on the approach of nucleic acid elements to one another, and the question of pairwise interhelical attraction with trivalent ions, outside of the context of a condensed DNA phase, has remained largely unexplored.

■ RESULTS

Disulfide Cross-Linking Assay to Measure Interhelical Encounters. For each set of linkers and conditions tested, we measured the second-order rate constant for cross-linking by using a fixed concentration of the thiol-containing helix and several concentrations of excess disulfide-containing helix (Figure 2C,D). Because helix−helix encounters are in rapid equilibrium relative to disulfide formation (see Supporting Information, *Establishment of Bounds on* k_{chem}), this second-order rate constant is the product of three steps. The concentration-dependent interhelical encounter equilibrium, K_{enc}, is the critical term of interest. The observed rate constant also depends on the cross-linking step, which is further separable into a pre-equilibrium term, K_a, representing deprotonation of the thiol, and a rate-limiting thiolate-dependent cross-linking term, k_{chem}. These steps are probed below to allow isolation of K_{enc} (Determination of the Salt Dependences of K_a and k_{chem}). Examination of the concentration-dependent cross-linking rate constants also revealed a small positive *y*-intercept (Figure 2D), which reflects a disulfide-independent reaction that inactivates the thiol with a rate constant that does not depend on salt identity or concentration across our experimental conditions and does not interfere with our measurements (Figure S4).
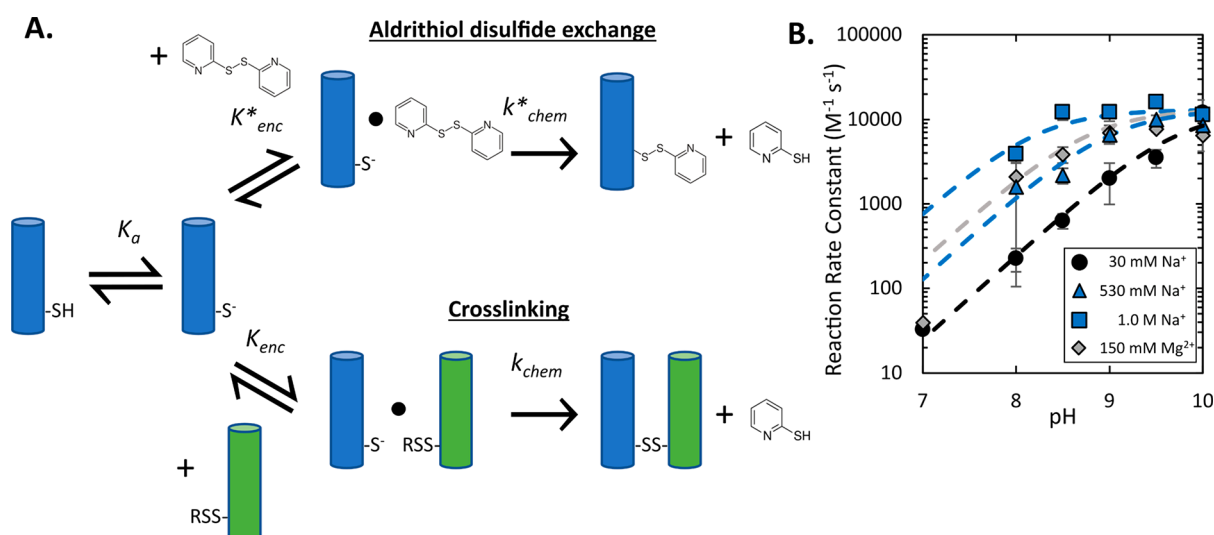
Figure 3. Reactions of the uncharged 2-aldrithiol to dissect effects of ions on thiol deprotonation and reaction and to provide a reference rate constant for cross-linking in the absence of electrostatic effects. (A) Scheme comparing the interhelical cross-linking reaction (bottom) to an analogous disulfide exchange reaction between the thiolated helix and 2-aldrithiol (top), which has the same chemical leaving group as in the cross-linking reactions. This product, 2-thiopyridine, is measured by absorbance at 343 nm (see Figure S5A). This disulfide exchange reaction captures the same reaction steps as cross-linking but with a salt-independent encounter equilibrium (K^*_{enc}). (B) Second-order rate constants for the 2-aldrithiol reaction as a function of pH for reactions with 30 mM Na$^+$ (black), 530 mM Na$^+$ (blue triangles), 1.0 M Na$^+$ (blue squares), or 150 mM Mg^{2+} (gray diamonds). Second-order rate constants were determined from at least three pseudo-first-order rate constant measurements. Data were collected at additional conditions (at pH values ≤10 to maintain stability of the DNA duplex), but for clarity, only the selected conditions are shown. The data were well described by a model (dashed curves) that gave salt-dependent thiol pK_a values and a single maximal rate constant ($k_{max} = 1.3 \times 10^4$ M^{-1} s^{-1}), indicating that k^*_{chem} is unaffected by salt concentration or identity across the ranges tested. The result that k_{max} is orders of magnitude smaller than the rate of diffusion (10^4 vs 10^9 M^{-1} s^{-1}) implies that K_{enc} is in rapid equilibrium relative to disulfide formation, and k_{chem} is therefore rate-limiting.

We measured second-order rate constants of cross-linking with various concentrations of Na$^+$, K$^+$ (30 mM to 1.0 M) and Mg^{2+} (0.1–300 mM in a background of 30 mM Na$^+$) and with different linker lengths (Figure 2E). The measured rate constants spanned about 2 orders of magnitude, from ~10^2 M^{-1} s^{-1} with short linkers and low monovalent ion concentration (30 mM Na$^+$, black dashed line) to ~10^4 M^{-1} s^{-1} with short linkers at ≥100 mM Mg^{2+} and long linkers at all conditions, suggesting that the assay is sensitive to electrostatics. As expected, higher salt concentrations gave higher cross-linking rates, and cross-linking rates were much higher with a given concentration of Mg^{2+} than monovalent ions (e.g., Figure 2E). The monovalent ions Na$^+$ and K$^+$ gave indistinguishable cross-linking (Figure 2E), consistent with the absence of a preference for Na$^+$ vs K$^+$ in the ion atmosphere.[19,30] These results match our general expectations about the salt concentration and valence dependence of the cross-linking rate and the sensitivity of this dependence to the interhelical separation distance.

Determination of the Salt Dependences of K_a and k_{chem}. As the raw second-order rate constants depend on all three of the reaction steps shown in Figure 2B, we performed a series of measurements to isolate the effects of salt concentration and identity on the frequency of helix encounters (K_{enc}). We expected that the negative electrostatic potential generated by the thiolated helix would disfavor thiol deprotonation, decreasing K_a (i.e., increasing the pK_a of the thiol), and that increasing the ionic strength would counter this effect.[32] As the thiolate is the reactive species, a shift in the pK_a results in a change in the amount of available reactant and must be accounted for. It was also possible that the salt concentration and identity would impact the chemical step of cross-linking (k_{chem}), though our results described below indicate that it does not.

To measure the pK_a shift and test for effects on k_{chem}, we used an analogous disulfide exchange reaction between the thiolated helix and an electrically neutral small molecule, 2-aldrithiol (Figures 3 and S5). Because 2-aldrithiol is uncharged, its encounter frequency with the thiolated helix (K^*_{enc}) is expected to be insensitive to the properties of the ion atmosphere. Thus, any changes in second-order rate constant of this disulfide exchange reaction (Figure 3A, top path) in response to changes in ionic conditions would arise from effects on thiol deprotonation (K_a) and/or the chemical step of this reaction (k^*_{chem}), which is the same chemistry as in our cross-linking reactions.

We found a log–linear relationship between the second-order rate constant and pH for the 2-aldrithiol reaction, as expected, with a plateau at high pH values (Figure 3B). We determined the pK_a value at each salt concentration by using a model with a single deprotonation event preceding the chemical step. As expected, the pK_a values were the highest at low salt concentrations (9.7 ± 0.1 at 30 mM Na$^+$) and decreased at high salt concentrations (8.2 ± 0.3 at 1.0 M Na$^+$ and 8.8 ± 0.3 at 150 mM Mg^{2+}; Figure S2F,G). In addition, the data across the varying salt concentrations were well described by a global model with a single maximal rate constant at the plateau (k_{max}) of 1.3×10^4 M^{-1} s^{-1}, indicating that k^*_{chem} is salt independent and simplifying our analyses. To independently determine the pK_a and maximal rate constant without perturbation from the helix electrostatic potential, we performed analogous disulfide exchange reactions with a small molecule thiol analogue (Figure S6). These reactions revealed the same plateau rate constant (1.3×10^4 M^{-1} s^{-1}) and gave a pK_a value of 8.5 ± 0.2, similar to the value for reactions of 2-aldrithiol with the helix at high ion concentrations. These results indicate that deprotonation of the thiol is disfavored by the electrostatic potential of the DNA, as
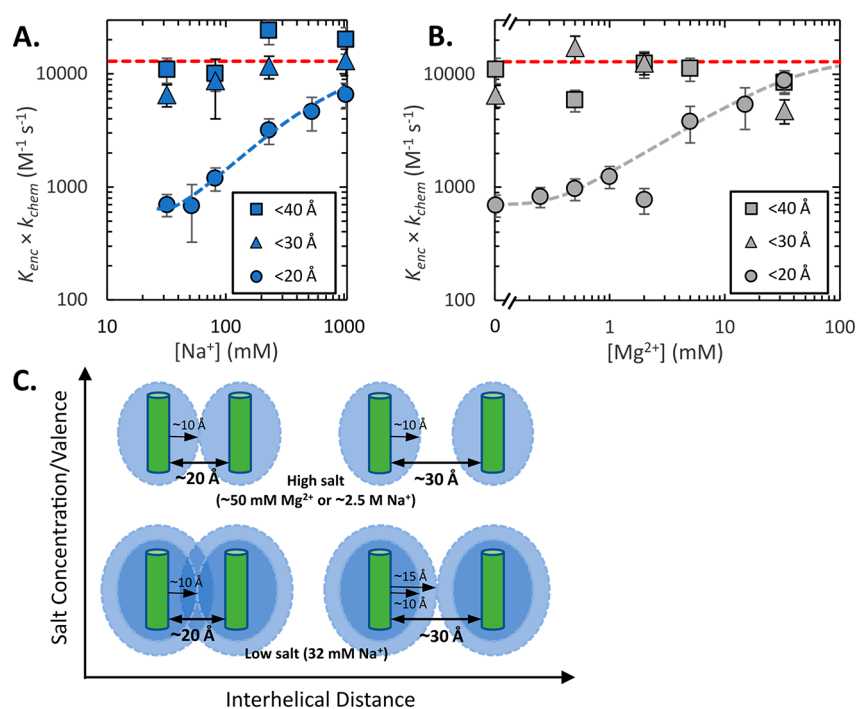
Figure 4. Encounter frequencies using various probe distances with (A) Na$^+$ and (B) Mg^{2+}. The red dashed lines correspond to k_{max}, the expected rate constant in the absence of electrostatic repulsion (diffusion-dominated encounters). Dashed curves are guides only. (C) Cartoon of energetics for interhelical approach. At low salt concentration (30 mM Na$^+$, bottom illustrations), effective screening is observed with 30-Å probe distances, indicating that the electrostatic potentials extend less than 15 Å from each helix. The repulsive potential of 1.8 kcal/mol observed with 20-Å probe separation (lower left) indicates overlap of the regions of enhanced potential from each helix. With high salt concentrations (top illustrations), complete screening is observed with the shortest measured distance of 20 Å, indicating that the potential extends less than 10 Å as shown.

expected, and that increased ionic strength mitigates this effect, ultimately decreasing the pK_a to a value indistinguishable from the small molecule reference.

With this information in hand, in the next section we return to the cross-linking results. We used the measured pK_a values to normalize for the fraction of thiolate at each salt concentration, removing any impact of K_a as a variable (see Materials and Methods and Supporting Information, Figure S7 and *Assessing the Impact of Helix Encounters on Observed* pK_a). Further, from the finding that k_{chem} does not depend on salt concentration or identity across the ranges tested, we can infer that changes to $K_{enc} \times k_{chem}$ measured in cross-linking reflect changes only in K_{enc}. Thus, we could unambiguously determine the effects of salt concentration and identity on K_{enc}, the encounter frequency between helices.

Changing Probe Lengths Reveals the Distance That the Electrostatic Potential Extends from a Helix. Using the cross-linking data in Figure 2 and the tools from the section above, we isolated effects on the helix encounter frequency (Figure 4). Across the range of Na$^+$ and Mg^{2+} concentrations tested, reactions probing distances up to 30 or 40 Å gave second-order rate constants ($K_{enc} \times k_{chem}$) that were the same within error as k_{max}, the maximal rate constant for the reaction with the uncharged 2-aldrithiol (Figure 4A,B, red dashed lines). Thus, the helices are not experiencing electrostatic repulsion, implying that their electrostatic potentials are fully screened at a combined distance of ≤30 Å.

For reactions using short linkers (probing interhelical separations of 20 Å), the values of $K_{enc} \times k_{chem}$ were lower and depended on salt concentration and identity (described further in the next section) while approaching the k_{max} value at high salt concentrations, indicating nearly full screening with ∼50 mM

Mg^{2+} or ∼2.5 M Na$^+$. These behaviors are qualitatively consistent with basic expectations for charge repulsion and screening, but they are quantitatively quite different from predictions using PB (see below).

The onset of the screened regime reveals the distance that the electrostatic potential extends away from the helix—i.e., the size of the region of electrostatic potential—and how this size depends on the ion concentration and identity (Figure 4C, Figure S8). At low ionic strength (30 mM Na$^+$), repulsion is observed for 20 Å separation but full screening is achieved for 30 Å separation. Thus, the electrostatic potential extends between 10 and 15 Å from each helix. As described further below, the repulsion observed for 20 Å separation is decreased with increasing ion concentrations until full screening is reached with ∼2.5 M Na$^+$ (by extrapolation from data up to 1 M Na$^+$) or 50 mM Mg^{2+}. Thus, under these conditions the size of the electrostatic potential is reduced so that it extends only ∼10 Å from the helix (Figure 4C). Our results indicate that for a broad range of conditions that span those found in cells, the potential extends between 10 and 15 Å from a DNA helix.

Evaluating the Energetic Penalty for Helix Encounters with ≤20 Å Separation. The cross-linking reactions probing 20 Å separation revealed information about the magnitude of the energetic penalty for overlapping potentials and how the penalty depends on salt concentration and identity (Figure 5A). At lower Mg^{2+} concentrations and across most of the tested range of Na$^+$ concentrations, the cross-linking rate constants were substantially smaller than k_{max}, implying a decreased value of K_{enc} due to electrostatic repulsion between the helices. At low ionic strength (30 mM Na$^+$) the rate constant for cross-linking was 20-fold below k_{max}, corresponding to an energetic penalty of 1.80 ± 0.14 kcal/mol for bringing the helices within 20 Å of each
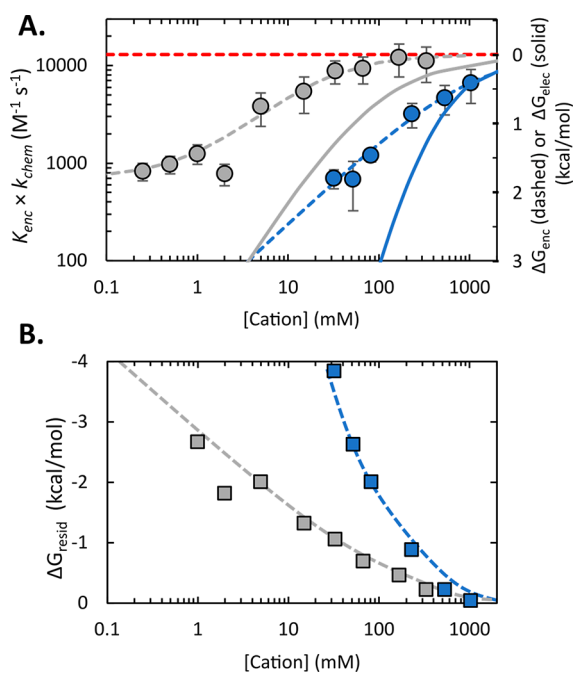
Figure 5. Salt concentration-dependent encounter frequencies and corresponding free energies. (A) Rate constants for cross-linking of the deprotonated thiolate and corresponding ΔG_{enc} values. Added cations are Na$^+$ (blue) and Mg^{2+} (gray) (with 30 mM Na$^+$ background), with experimental data shown as points, dashed curves showing logistic function best fits, and solid curves showing corresponding ensemble PB calculations of the electrostatic free energy, ΔG_{elec}. Figure S9 provides PB calculations at specific interhelical orientations. Logistic fits to the data yielded slopes of 0.87 CI$_{95}$(0.68, 1.15) for Na$^+$ and 0.96 CI$_{95}$(0.78, 1.22) for Mg^{2+}. Logistic fits to the predictions made by PB yielded slopes of 2.80 CI$_{95}$(2.62, 2.98) for Na$^+$ and 1.28 CI$_{95}$(1.24, 1.31) for Mg^{2+}. Measurements were at pH 9.0 with 100 mM Na-CHES (30 mM background Na$^+$). Error bars are SE and reflect the propagated uncertainty from interhelical and 2-aldrithiol reaction rate constants. The red dashed line corresponds to k_{max}, the rate constant in the absence of electrostatic repulsion. Values of ΔG_{enc} are relative to this reference reaction. (B) The residual free energy ΔG_{resid} (squares, colors as in panel A), defined as the difference between the observed free energy of encounters ΔG_{enc} and the electrostatic free energy calculated by PB, ΔG_{elec}. Because $\Delta G_{elec} > \Delta G_{enc}$ across our solution conditions, $\Delta G_{resid} \leq 0$, favoring interhelical encounters. Dashed curves are guides only.

other (10 Å away from each helix). From the results in the previous section, we know that the potential extends ≤ 15 Å from each helix under these conditions. Thus, the boundary of the ion atmosphere is quite sharp, with a 1.8 kcal/mol penalty for overlapping the electrostatic potentials by just a few angstroms, a distance smaller than an ionic hydration shell.

We found that the magnitude of the energetic penalty depends strongly on both concentration and valence of salt, with K_{enc} increasing log–linearly with Na$^+$ or Mg^{2+} concentration (Figure 5A). Across this log–linear regime, spanning 2 orders of magnitude in concentration for each salt, 40–80-fold more Na$^+$ than Mg^{2+} is required to achieve the same degree of electrostatic screening. This difference in screening efficiency is substantially larger than the 10–13-fold preference for Mg^{2+} over Na$^+$ in the occupancy of the ion atmosphere,[19,30] perhaps because Mg^{2+} ions associate with the DNA helical surface at smaller distances than do Na$^+$ ions.[32,63,64] A denser, more confined ion atmosphere with Mg^{2+} as the dominant counterion is predicted

to yield smaller electrostatic potentials at a given distance from the helix than a more diffuse ion atmosphere composed primarily of Na$^+$ (Figure 1C).

To test whether the free energy penalty ΔG_{enc} was aligned with the simple formulation of electrostatics provided by PB, we performed calculations to generate predicted free energy penalties from electrostatic repulsion, ΔG_{elec} (see Supporting Information, Figure S9 and *Poisson−Boltzmann Calculations of ΔG_{elec}*.) We found that the predicted penalties were much larger than our measured penalties across wide ranges of salt concentrations, and with much larger dependences on ion concentrations, such that the differences were largest at low ion concentrations (Figure 5A, dashed curves vs points). For all ionic conditions tested, the difference between the experimental and computational results, ΔG_{resid}, is favorable (i.e., <0; Figure 5B), raising the possibility that an attractive force ameliorates the net repulsion and is largest at low ion concentrations.

Trivalent Cobalt Hexamine Induces an Attractive Potential between Isolated DNA Helices. The prior results demonstrating condensation of DNA in the presence of Co(NH$_3$)$_6^{3+}$ or other trivalent cations suggested an attractive force between helices, but the high concentrations of DNA required and the large condensates prevented quantitative analysis of any pairwise attraction between helices and raised the possibility that higher-order cooperativity between DNA segments was required for attraction. Our cross-linking approach provided an opportunity to probe directly whether Co(NH$_3$)$_6^{3+}$ results in an attraction between two isolated helices, which would result in a cross-linking rate that is even larger than that for the fully screened condition, and an opportunity to measure this attraction, if present.

Therefore, we measured interhelical cross-linking in the presence of various concentrations of Co(NH$_3$)$_6^{3+}$ (Figure 6).
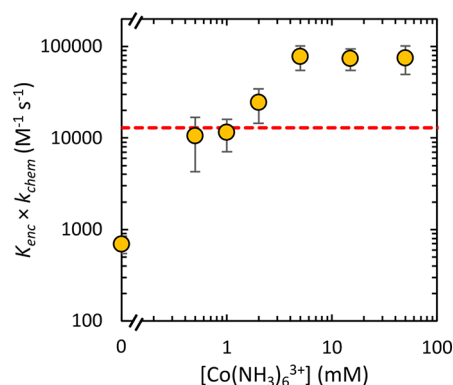
Figure 6. Trivalent salt Co(NH$_3$)$_6^{3+}$ overcomes repulsion and induces a net attractive force between helices. The plot shows thiolate second-order cross-linking rate constants measured with various Co(NH$_3$)$_6^{3+}$ concentrations. Error bars reflect SE and include the propagated uncertainty from interhelical and 2-aldrithiol reaction rate constants. The red dashed line corresponds to k_{max}, the rate constant in the absence of electrostatic effects.

For separations of up to 20 Å, the lowest concentration tested, 0.5 mM Co(NH$_3$)$_6^{3+}$, gave the second-order rate constant k_{max}, indicating full screening. However, instead of reaching a plateau at this value, higher concentrations of Co(NH$_3$)$_6^{3+}$ further increased the rate constant, to a value nearly 10-fold larger. Thus, Co(NH$_3$)$_6^{3+}$ induces a net attractive pairwise potential between DNA helices at a range ≤ 20 Å. The onset and magnitude of this attraction are largely unaffected by probe

length (Figure S10), suggesting a free energy minimum at ≤20 Å between the helices. Cross-linking rates remain second-order with DNA concentration across the attractive regime, (Figure S11), suggesting that we are capturing a strictly pairwise interaction. This attractive force has a magnitude of −1.2 ± 0.3 kcal/mol for our 15-bp helices (0.13 ± 0.03 kT/bp).

DISCUSSION

We developed an interhelical cross-linking assay, xHEED, to examine energetic interactions between DNA helices, and we used it to directly measure the free energy change experienced by two helices as they approach each other. In the presence of monovalent and divalent ions, we measured how far the electrostatic repulsion—and therefore the electrostatic potential—extends from the helices. In the presence of the trivalent ion $Co(NH_3)_6^{3+}$ we detected and quantitated an attractive force between two helices in solution.

Our results show that the electrostatic potential surrounding a DNA helix extends between 10 and 15 Å across physiologically relevant ionic conditions. Bringing two helices (15 bp each) together to a distance just a few angstroms inside of this boundary incurs a free energy penalty of nearly 2 kcal/mol. In cells, DNA genomes in cell nuclei and virus particles are packed much closer together, and over much larger helical lengths, suggesting that these helices experience substantial repulsive forces. These forces are apparently overcome by additional factors, most prominently by nucleic acid-binding proteins that substantially alter the electrostatic potential. Recent detailed studies of the electrostatics of nucleosomes[2] and DNA bound to a transcription factor[65] highlight radical changes to the ion atmospheres of bound nucleic acids. Nevertheless, these nucleic acids retain strong negative electrostatic potentials, suggesting that additional factors must also contribute.

In this regard, it is striking that the energetic penalty for interhelical approach at low ion concentrations, while significant, is much smaller than expected from simple consideration of the electrostatics by Poisson−Boltzmann modeling. In general, PB modeling is in qualitative agreement with the results and accurately predicts the salt concentrations required for full screening (100 mM Mg^{2+} or 2 M Na^+; see Figure 5A). However, it predicts a much larger dependence of the energy barrier on salt concentrations than observed, such that at low to moderate salt concentrations, helix encounters occur 2-to-3 orders of magnitude more frequently than predicted by PB. It is interesting that PB overestimates the repulsion by such a wide margin, as it is able to predict the number of ions and the composition of the ion atmosphere under similar conditions.[19,28]

To consider possible sources of the difference between the PB predictions and experimental results, it is important to recognize that PB is a mean-field approach and lacks specific ion positions. Thus, the difference between the observations and predictions most likely stems from atomic features of the ions and/or the solvent that produce an attractive force component, which opposes the electrostatic repulsion. Electrostatic ordering of ions[61] or water[66] in the ion atmosphere could give entropic effects favoring interhelical approach consistent with our observations, and both have previously been proposed as sources of attraction.[61,66] Attractive hydration forces[55,60,66] and ion−ion correlations[67] have been proposed as sources for net attraction in the context of multivalent cation-induced DNA condensation, and it is possible that these phenomena contribute to mitigating interhelical repulsion with mono- and divalent cations. Regardless of its origin, this attractive effect represents an important tool that nature can exploit to facilitate nucleic acid compaction in the face of what would otherwise be extremely large repulsive force between helices.

The net attraction that we observed between DNA helices in the presence of the trivalent ion $Co(NH_3)_6^{3+}$ builds on previous observations of trivalent ion-dependent DNA condensation,[52−55,60] where the high DNA concentrations necessary to observe condensation complicated quantitative studies and suggested that higher-order cooperativity might be necessary. We find that the magnitude of the potential at low DNA concentrations is in the range of previous estimates (∼0.1−0.2 kT/bp[20,55,60]), and our interhelical separation at the free energy minimum is consistent with a previous estimate of 8 to 12 Å for the interhelical separation in $Co(NH_3)_6^{3+}$-condensed DNA.[55] The similarity of these parameters suggests that the net pairwise attractive potential at low DNA concentrations also underlies the condensation at higher DNA concentrations. Thus, cooperativity may not be a significant contributor, implying that the high concentrations in previous studies were required simply to achieve DNA concentrations above the equilibrium dissociation constant for the condensation process.

The quantitative cross-linking method developed here, xHEED, has great potential for building further understanding of nucleic acid energetics. The linkers can be systematically varied to probe both longer and shorter interhelical distances, extending the quantitative information on the distance dependence of interhelical repulsion in monovalent and divalent ions. Analogous experiments can be performed with RNA, to probe reported differences between DNA and RNA in polyvalent ions and to learn more about RNA folding. It will also be of interest to probe further the net attraction in trivalent ions by testing biologically relevant polyamines. xHEED can also be applied in the presence of proteins or with nucleosomes to address the ways that biology modulates electrostatic potentials and overcomes repulsion. Perhaps most generally, xHEED provides a new vantage point for examining nucleic acid electrostatics, generating results that can provide critical tests of widely used models like PB and will serve as key points of reference for continued development of new theoretical and computational approaches to model nucleic acid structures and compaction.

MATERIALS AND METHODS

Disulfide- and Thiol-Modified DNA Preparation. Oligonucleotides (Integrated DNA Technologies) with C5-amino-dT modifications at specific positions (IHO114, IHO116, IHO347, IHO343) were suspended to ∼500 μM in 20 mM Na-borate, 1.0 mM EDTA at pH 8.0. Prior to reaction, fresh 100 mM SPDP or LC-SPDP (Thermo Fisher) was prepared in DMSO. Reactions (80 μL) were prepared with 100 mM Na-borate pH 8.0, 20 mM SPDP/LC-SPDP, and ∼200 μM oligonucleotide, and incubated 50 min at 37 °C. Reactions to produce disulfide modifications (IHO114, IHO347) were then placed on ice, and reactions intended for thiol modifications (IHO116, IHO343) had 10 μL 1.0 M DTT added and were incubated for an additional 45 min. Modified oligonucleotides were purified by buffer exchange with 50 mM MOPS pH 5.8 in Amicon Ultra 3K 0.5 mL concentrators (Sigma). Final elution volumes were 40−50 μL, and concentration was determined by measuring absorbance at 260 nm (A_{260}). Thiol activity was quantitated by stoichiometric reaction with 2-aldrithiol (see below, Spectrophotometric Disulfide Exchange Assay), and found to range consistently at 50−65%.

5′ DNA Radiolabeling by T4 Polynucleotide Kinase. Oligonucleotides (IDT) (IHO117, IHO340) were initially diluted to ∼50 μM in 10 mM Tris, 1.0 mM EDTA at pH 8.0 (TE). Labeling reactions (5 μL) were performed by adding 1 μL of $[\gamma\text{-}^{32}P]ATP$ (150

mCi/mL, PerkinElmer) to 50 pmol oligonucleotide with 10 activity units of T4 polynucleotide kinase (New England Biolabs) in NEB T4 PNK buffer and incubating for 1 h at 37 °C. Radiolabeled DNA was purified from the reaction mixture by 12% native PAGE or by using a Zymo Oligo Clean and Concentrator Kit (Zymo Research). Activity was quantitated by scintillation counting. Experiments repeated with preparations using each purification method yielded indistinguishable results.

PAGE-Resolved Disulfide Cross-Link Assay. Disulfide- and thiol-modified DNA helices were prepared separately in 10 mM NaOAc pH 4.5. The disulfide helix mixture was prepared with the disulfide-modified oligonucleotide (IHO114 or IHO347) and its complement (IHO115 or IHO345, respectively) in a 1:2 ratio at a concentration of either 10 or 20 μM disulfide. The thiol helix mixture was prepared with 100 nM thiol-modified oligonucleotide (IHO116 or IHO343) and radiolabeled complement (IHO117 or IHO340, respectively) at an activity of ≈10^4 dpm/μL (<1 nM). Each mixture was briefly incubated at 70 °C.

Prereactions (10 μL) were initially assembled in 10 mM NaOAc, pH 4.5, by combining 2 μL of the thiolated helix mixture prepared above with varying amounts of the disulfide helix mixture. Cross-linking was undetectably slow at this pH. Reactions were briefly preheated to 37 °C, and then cross-linking was initiated by shifting the pH by rapid addition of 10 μL of start buffer (200 mM CHES, pH 9.0, and a 2× concentration of chloride salts of Na$^+$, K$^+$, Mg^{2+}, or Co(NH$_3$)$_6$$^{3+}$). Upon initiation, reactions were 20 μL with 5.0 mM NaOAc, 100 mM CHES pH 9.0, <100 pM thiolated radiolabeled helix at 1000 dpm/μL, 50 nM to 8 μM disulfide helix, and salt concentrations as indicated.

Reactions were incubated at 37 °C, and at specified time points, 2 μL reaction samples were transferred to 8 μL of acid quench buffer (50% glycerol, 150 mM NaOAc, pH 4.5, and 0.1% bromophenol blue) on ice. Samples were resolved by 12% native PAGE. Gels were dried, exposed on a phosphorimager screen overnight, and scanned using a Typhoon FLA 9500 (GE Healthcare). Data were quantified using ImageQuant 5.2 (GE Healthcare). Additional analysis and fitting were performed using Excel (Microsoft), Matlab (Mathworks), and Python scripting.

Spectrophotometric Disulfide Exchange Assay. A 10 mM 2-aldrithiol (Sigma) stock was prepared in water. Thiolated DNA helix mixture was prepared in 10 mM NaOAc, pH 4.5, by combining thiolated oligonucleotide (IHO116 or IHO343) and its unlabeled complement (IHO117 or IHO340, respectively) in a 1:1.1 ratio at a concentration of 6 μM thiol, then heating briefly at 70 °C and placing on ice. 4×-concentrated solutions of 2-aldrithiol were prepared in water, with 1× concentrations from 10 to 100 μM. Buffer solutions (2×) were prepared with 200 mM buffer and various concentrations of salts. Buffers used were Na-MOPS at pH 7.0 and 7.5, Na-Tris or Na-EPPS at pH 8.0 and 8.5, Na-CHES at pH 9.0 and 9.5, and Na-CAPS at pH 10.0.

Reactions (60 μL) were performed in a 100-μL-capacity quartz cuvette by adding 30 μL of 2× buffer solution, followed by 15 μL of a 4× 2-aldrithiol solution. The cuvette was then placed inside a DU 800 spectrophotometer (Beckman Coulter) set to record A_{343} over time at 1.5 s intervals. The reaction was started by the rapid addition of 15 μL of the thiolated DNA duplex mixture.

Disulfide Exchange with Small Molecule Thiol Analogue. Buffers and 2-aldrithiol solutions were prepared as above. A 2.0 mM *N*-phenyl-3-sulfanylpropanamide (Key Organics) stock (NPSP) was prepared in 1% DMSO. This stock was subsequently diluted to 6 μM NPSP in 10 mM NaOAc, pH 4.5. Disulfide exchange reactions between NPSP and 2-aldrithiol were performed as described above with 6 μM NPSP in place of 6 μM thiolated DNA.

Measurement of Inactivating Side Reaction. Chemically modified helices were prepared as above. Trace radiolabeled thiol helix was incubated alone at 37 °C in 100 mM Na-CHES pH 9.0 with varying salts. At specific time points, 2 μL samples were combined with 2 μL of 8 μM disulfide helix at pH 9.0 and 2 M NaCl. These were incubated at 37 °C for an additional 30 min to allow cross-linking to proceed to completion, moved to ice, and 16 μL of acid quench buffer was added to each sample. Samples were resolved by 12% native PAGE as above.

Cross-Linking Rate Data Normalization. To account for salt effects on the pre-equilibrium thiol deprotonation step (K_a), second-order rate constants were measured for disulfide exchange with 2-aldrithiol at several salt concentrations with buffer conditions identical with those used in interhelical cross-linking. Since we established that k_{chem} was not affected by salt concentration or identity, and the maximal disulfide exchange rate k_{max} was measured when the thiol is expected to be deprotonated in the ground state, we obtained the fractional deprotonation of the thiol f_{deprot} across salt concentrations by dividing 2-aldrithiol disulfide exchange rates by k_{max}. Because deprotonation is expected to be a rapid equilibrium, an observed second-order cross-linking rate is related to the encounter equilibrium (K_{enc}) by the expression:

$$k_{obs} = f_{deprot} \times K_{enc} \times k_{chem}$$

Thus, to remove salt effects on the deprotonation step from consideration, we divided each observed cross-linking rate constant by the fractional thiol deprotonation, leaving us with just $K_{enc} \times k_{chem}$.

In practice, 2-aldrithiol disulfide exchange data were not collected at all of the salt conditions used in cross-linking, so empirical curve fits were performed to estimate fractional thiol deprotonation across salt concentrations (Figure S12).

Poisson–Boltzmann Calculations of ΔG_{elec}. Poisson–Boltzmann calculations were performed using APBS.[68−70] For calculating ΔG_{elec}, PyMol[71] was used to prepare .pqr files containing two 15-bp DNA helices in four orientations with separations ranging from 4 to 30 Å. A single helix was used as an infinite dilution reference state. APBS's automatic finite difference multigrid method was used with a coarse grid size of 130 × 130 × 215 Å, a fine grid size of 105 × 105 × 185 Å, and grid dimensions of 193 × 193 × 321. Single Debye−Hückel method was used for boundary conditions. Finer grid dimensions or larger box sizes did not substantially affect results. Dielectric constants were set to 75 and 2.0 in the solvent and molecular interior, respectively. Other parameters were set to default values recommended in APBS documentation. Values of ΔG were calculated as the difference between the electrostatic energy for some orientation, separation, and salt concentration and twice the energy for the isolated helix at the same salt concentration. Artifactual self-energies were removed by re-referencing ΔG to a saturated Na$^+$ condition. Ensemble energies were calculated as the Boltzmann-weighted average of energies calculated across helix orientations. The ionic contribution from buffer was explicitly included in all calculations to replicate experimental conditions.

Self-Avoiding Walk Model of Linker Chains. A self-avoiding walk (SAW) model was implemented in Python to model the distribution of linker chain ends. This program generated freely rotating self-avoiding chains with a fixed bond angle, bond length, and segment diameter (Figure S2A). A growth algorithm was employed which iteratively attempted to add an additional chain segment to a nascent chain, checking whether each new segment intersected with any other segment in the chain, or with an impenetrable planar surface located at the chain origin. If an intersection occurred, the chain was discarded, and growth was restarted from the origin. If a chain reached its full length, the location of its terminus was output to a file. For chains of 14 segments, 27 693 chain configurations were generated from 2.5 × 10^8 attempted growths. The locations of the chain ends were binned to produce a histogram estimate of the probability distribution function of chain extensions.

DNA Sequences. Oligonucleotides purchased from IDT are shown in Table S1.

■ ASSOCIATED CONTENT

Ⓢ Supporting Information

The Supporting Information is available free of charge at https://pubs.acs.org/doi/10.1021/jacs.1c11122.

> Additional experimental details, analysis, and discussion; Table S1; Figures S1−S13 (PDF)

■ AUTHOR INFORMATION

Corresponding Author

   Rick Russell − *Department of Molecular Biosciences, University of Texas at Austin, Austin, Texas 78712, United States;* ◉ orcid.org/0000-0002-4879-8563; Email: rick_russell@cm.utexas.edu

Authors

   Ian Hamilton − *Department of Molecular Biosciences, University of Texas at Austin, Austin, Texas 78712, United States;* ◉ orcid.org/0000-0002-6217-9013

   Magdalena Gebala − *Department of Biochemistry, Stanford University, Stanford, California 94305, United States*

   Daniel Herschlag − *Department of Biochemistry, Stanford University, Stanford, California 94305, United States;* ◉ orcid.org/0000-0002-4685-1973

Complete contact information is available at:
https://pubs.acs.org/10.1021/jacs.1c11122

Notes

The authors declare no competing financial interest.

■ ACKNOWLEDGMENTS

■ REFERENCES

(1) Fenley, A. T.; Adams, D. A.; Onufriev, A. V. Charge State of the Globular Histone Core Controls Stability of the Nucleosome. *Biophys. J.* **2010**, *99* (5), 1577−1585.

(2) Gebala, M.; Johnson, S. L.; Narlikar, G. J.; Herschlag, D. Ion Counting Demonstrates a High Electrostatic Field Generated by the Nucleosome. *eLife* **2019**, *8*, No. e44993.

(3) Shakya, A.; Park, S.; Rana, N.; King, J. T. Liquid-Liquid Phase Separation of Histone Proteins in Cells: Role in Chromatin Organization. *Biophys. J.* **2020**, *118* (3), 753−764.

(4) Gibson, B. A.; Doolittle, L. K.; Schneider, M. W. G.; Jensen, L. E.; Gamarra, N.; Henry, L.; Gerlich, D. W.; Redding, S.; Rosen, M. K. Organization of Chromatin by Intrinsic and Regulated Phase Separation. *Cell* **2019**, *179* (2), 470−484.

(5) Fuller, D. N.; Rickgauer, J. P.; Jardine, P. J.; Grimes, S.; Anderson, D. L.; Smith, D. E. Ionic Effects on Viral DNA Packaging and Portal Motor Function in Bacteriophage 29. *Proc. Natl. Acad. Sci. U. S. A.* **2007**, *104* (27), 11245−11250.

(6) Belyi, V. A.; Muthukumar, M. Electrostatic Origin of the Genome Packing in Viruses. *Proc. Natl. Acad. Sci. U.S.A.* **2006**, *103* (46), 17174−17178.

(7) Draper, D. E. A Guide to Ions and RNA Structure. *RNA* **2004**, *10* (3), 335−343.

(8) Stein, A.; Crothers, D. M. Equilibrium Binding of Magnesium(II) by Escherichia Coli TRNAfMet. *Biochemistry* **1976**, *15* (1), 157−160.

(9) Misra, V. K.; Draper, D. E. The Linkage between Magnesium Binding and RNA Folding. *J. Mol. Biol.* **2002**, *317* (4), 507−521.

(10) Takamoto, K.; Das, R.; He, Q.; Doniach, S.; Brenowitz, M.; Herschlag, D.; Chance, M. R. Principles of RNA Compaction: Insights from the Equilibrium Folding Pathway of the P4-P6 RNA Domain in Monovalent Cations. *J. Mol. Biol.* **2004**, *343* (5), 1195−1206.

(11) Grilley, D.; Soto, A. M.; Draper, D. E. Mg2+−RNA Interaction Free Energies and Their Relationship to the Folding of RNA Tertiary Structures. *Proc. Natl. Acad. Sci. U.S.A.* **2006**, *103* (38), 14003−14008.

(12) Leipply, D.; Lambert, D.; Draper, D. E. Ion−RNA Interactions. In *Methods in Enzymology*; Elsevier, 2009; Vol. *469*, pp 433−463. DOI: 10.1016/S0076-6879(09)69021-2.

(13) Shi, Y.-Z.; Jin, L.; Wang, F.-H.; Zhu, X.-L.; Tan, Z.-J. Predicting 3D Structure, Flexibility, and Stability of RNA Hairpins in Monovalent and Divalent Ion Solutions. *Biophys. J.* **2015**, *109* (12), 2654−2665.

(14) Wang, J.; Karki, C.; Xiao, Y.; Li, L. Electrostatics of Prokaryotic Ribosome and Its Biological Implication. *Biophys. J.* **2020**, *118* (5), 1205−1212.

(15) Jayaram, B.; Sharp, K. A.; Honig, B. The Electrostatic Potential of B-DNA. *Biopolymers* **1989**, *28* (5), 975−993.

(16) Manning, G. S. Limiting Laws and Counterion Condensation in Polyelectrolyte Solutions II. Self-Diffusion of the Small Ions. *J. Chem. Phys.* **1969**, *51* (3), 934−938.

(17) Sharp, K. A.; Honig, B. Salt Effects on Nucleic Acids. *Curr. Opin. Struct. Biol.* **1995**, *5* (3), 323−328.

(18) Eisenberg, B. Interacting Ions in Biophysics: Real Is Not Ideal. *Biophys. J.* **2013**, *104* (9), 1849−1866.

(19) Bai, Y.; Greenfeld, M.; Travers, K. J.; Chu, V. B.; Lipfert, J.; Doniach, S.; Herschlag, D. Quantitative and Comprehensive Decomposition of the Ion Atmosphere around Nucleic Acids. *J. Am. Chem. Soc.* **2007**, *129* (48), 14981−14988.

(20) Bai, Y.; Das, R.; Millett, I. S.; Herschlag, D.; Doniach, S. Probing Counterion Modulated Repulsion and Attraction between Nucleic Acid Duplexes in Solution. *Proc. Natl. Acad. Sci. U.S.A.* **2005**, *102* (4), 1035−1040.

(21) Rau, D. C.; Lee, B.; Parsegian, V. A. Measurement of the Repulsive Force between Polyelectrolyte Molecules in Ionic Solution: Hydration Forces between Parallel DNA Double Helices. *Proc. Natl. Acad. Sci. U. S. A.* **1984**, *81* (9), 2621−2625.

(22) Pitt, S. W.; Zhang, Q.; Patel, D. J.; Al-Hashimi, H. M. Evidence That Electrostatic Interactions Dictate the Ligand-Induced Arrest of RNA Global Flexibility. *Angewandte Chemie - International Edition* **2005**, *44* (22), 3412−3415.

(23) Lipfert, J.; Sim, A. Y. L.; Herschlag, D.; Doniach, S. Dissecting Electrostatic Screening, Specific Ion Binding, and Ligand Binding in an Energetic Model for Glycine Riboswitch Folding. *RNA* **2010**, *16* (4), 708−719.

(24) Re, A.; Joshi, T.; Kulberkyte, E.; Morris, Q.; Workman, C. T. RNA−Protein Interactions: An Overview. In *RNA Sequence, Structure, and Function: Computational and Bioinformatic Methods*; Gorodkin, J., Ruzzo, W. L., Eds.; Methods in Molecular Biology; Humana Press: Totowa, NJ, 2014; pp 491−521. DOI: 10.1007/978-1-62703-709-9_23.

(25) Shazman, S.; Mandel-Gutfreund, Y. Classifying RNA-Binding Proteins Based on Electrostatic Properties. *PLOS Computational Biology* **2008**, *4* (8), No. e1000146.

(26) Krakauer, H. The Binding of Mg++ Ions to Polyadenylate, Polyuridylate, and Their Complexes. *Biopolymers* **1971**, *10* (12), 2459−2490.

(27) Römer, R.; Hach, R. TRNA Conformation and Magnesium Binding. *Eur. J. Biochem.* **1975**, *55* (1), 271−284.

(28) Gebala, M.; Herschlag, D. Quantitative Studies of an RNA Duplex Electrostatics by Ion Counting. *Biophys. J.* **2019**, *117* (6), 1116−1124.

(29) Gebala, M.; Giambaşu, G. M.; Lipfert, J.; Bisaria, N.; Bonilla, S.; Li, G.; York, D. M.; Herschlag, D. Cation-Anion Interactions within the Nucleic Acid Ion Atmosphere Revealed by Ion Counting. *J. Am. Chem. Soc.* **2015**, *137* (46), 14705−14715.

(30) Gebala, M.; Bonilla, S.; Bisaria, N.; Herschlag, D. Does Cation Size Affect Occupancy and Electrostatic Screening of the Nucleic Acid Ion Atmosphere? *J. Am. Chem. Soc.* **2016**, *138* (34), 10925−10934.

(31) Das, R.; Mills, T. T.; Kwok, L. W.; Maskel, G. S.; Millett, I. S.; Doniach, S.; Finkelstein, K. D.; Herschlag, D.; Pollack, L. Counterion Distribution around DNA Probed by Solution X-Ray Scattering. *Phys. Rev. Lett.* **2003**, *90* (18), 188103.

(32) Allred, B. E.; Gebala, M.; Herschlag, D. Determination of Ion Atmosphere Effects on the Nucleic Acid Electrostatic Potential and Ligand Association Using AH+·C Wobble Formation in Double-Stranded DNA. *J. Am. Chem. Soc.* **2017**, *139* (22), 7540−7548.

(33) Bai, Y.; Chu, V. B.; Lipfert, J.; Pande, V. S.; Herschlag, D.; Doniach, S. Critical Assessment of Nucleic Acid Electrostatics via Experimental and Computational Investigation of an Unfolded State Ensemble. *J. Am. Chem. Soc.* **2008**, *130* (37), 12334−12341.

(34) Borukhov, I.; Andelman, D.; Orland, H. Steric Effects in Electrolytes: A Modified Poisson-Boltzmann Equation. *Phys. Rev. Lett.* **1997**, *79* (3), 435−438.

(35) Grosberg, A. Yu.; Nguyen, T. T.; Shklovskii, B. I. Colloquium: The Physics of Charge Inversion in Chemical and Biological Systems. *Rev. Mod. Phys.* **2002**, *74* (2), 329−345.

(36) Nishio, T.; Minakata, A. Effects of Ion Size and Valence on Ion Distribution in Mixed Counterion Systems of Rodlike Polyelectrolyte Solution. I. Mixed-Size Counterion Systems with Same Valence. *J. Chem. Phys.* **2000**, *113* (23), 10784−10792.

(37) Nishio, T.; Minakata, A. Effects of Ion Size and Valence on Ion Distribution in Mixed Counterion Systems of a Rodlike Polyelectrolyte Solution. 2. Mixed-Valence Counterion Systems. *J. Phys. Chem. B* **2003**, *107* (32), 8140−8145.

(38) Lyubartsev, A. P.; Nordenskiöld, L. Monte Carlo Simulation Study of DNA Polyelectrolyte Properties in the Presence of Multivalent Polyamine Ions. *J. Phys. Chem. B* **1997**, *101* (21), 4335−4342.

(39) Chu, V. B.; Bai, Y.; Lipfert, J.; Herschlag, D.; Doniach, S. Evaluation of Ion Binding to DNA Duplexes Using a Size-Modified Poisson-Boltzmann Theory. *Biophys. J.* **2007**, *93* (9), 3202−3209.

(40) Giambaşu, G. M.; Luchko, T.; Herschlag, D.; York, D. M.; Case, D. A. Ion Counting from Explicit-Solvent Simulations and 3D-RISM. *Biophys. J.* **2014**, *106* (4), 883−894.

(41) Giambaşu, G. M.; Gebala, M. K.; Panteva, M. T.; Luchko, T.; Case, D. A.; York, D. M. Competitive Interaction of Monovalent Cations with DNA from 3D-RISM. *Nucleic Acids Res.* **2015**, *43* (17), 8405−8415.

(42) Sushko, M. L.; Thomas, D. G.; Pabit, S. A.; Pollack, L.; Onufriev, A. V.; Baker, N. A. The Role of Correlation and Solvation in Ion Interactions with B-DNA. *Biophys. J.* **2016**, *110* (2), 315−326.

(43) Lai, C.-L.; Chen, C.; Ou, S.-C.; Prentiss, M.; Pettitt, B. M. Interactions between Identical DNA Double Helices. *Phys. Rev. E* **2020**, *101* (3), No. 032414.

(44) Cohen, S. B.; Cech, T. R. Dynamics of Thermal Motions within a Large Catalytic RNA Investigated by Cross-Linking with Thiol-Disulfide Interchange. *J. Am. Chem. Soc.* **1997**, *119* (27), 6259−6268.

(45) Cohen, S. B.; Cech, T. R. A Quantitative Study of the Flexibility Contributed to RNA Structures by Nicks and Single-Stranded Gaps. *Rna* **1998**, *4* (10), 1179−1185.

(46) Fogolari, F.; Brigo, A.; Molinari, H. The Poisson−Boltzmann Equation for Biomolecular Electrostatics: A Tool for Structural Biology. *Journal of Molecular Recognition* **2002**, *15* (6), 377−392.

(47) Lipfert, J.; Doniach, S.; Das, R.; Herschlag, D. Understanding Nucleic Acid-Ion Interactions. *Annu. Rev. Biochem.* **2014**, *83*, 813−841.

(48) Feynman, R. P.; Leighton, R. B.; Sands, M. *The Feynman Lectures on Physics*; Addison-Wesley, 1964; Vol. 2.

(49) Galamba, N. Water's Structure around Hydrophobic Solutes and the Iceberg Model. *J. Phys. Chem. B* **2013**, *117* (7), 2153−2159.

(50) Juurinen, I.; Pylkkänen, T.; Sahle, C. J.; Simonelli, L.; Hämäläinen, K.; Huotari, S.; Hakala, M. Effect of the Hydrophobic Alcohol Chain Length on the Hydrogen-Bond Network of Water. *J. Phys. Chem. B* **2014**, *118* (29), 8750−8755.

(51) Hande, V. R.; Chakrabarty, S. Structural Order of Water Molecules around Hydrophobic Solutes: Length-Scale Dependence and Solute−Solvent Coupling. *J. Phys. Chem. B* **2015**, *119* (34), 11346−11357.

(52) Andresen, K.; Qiu, X.; Pabit, S. A.; Lamb, J. S.; Park, H. Y.; Kwok, L. W.; Pollack, L. Mono- and Trivalent Ions around DNA: A Small-Angle Scattering Study of Competition and Interactions. *Biophys. J.* **2008**, *95* (1), 287−295.

(53) Widom, J.; Baldwin, R. L. Cation-Induced Toroidal Condensation of DNA: Studies with Co3+(NH3)6. *J. Mol. Biol.* **1980**, *144* (4), 431−453.

(54) Widom, J.; Baldwin, R. L. Monomolecular Condensation of λ-DNA Induced by Cobalt Hexammine. *Biopolymers* **1983**, *22* (6), 1595−1620.

(55) Rau, D. C.; Parsegian, V. A. Direct Measurments of the Intermolecular Forces between Counterion-Condensed DNA Double Helices. *Biophys. J.* **1992**, *61* (1), 246−259.

(56) Gosule, L. C.; Schellman, J. A. Compact Form of DNA Induced by Spermidine. *Nature* **1976**, *259* (5541), 333−335.

(57) Gosule, L. C.; Schellman, J. A. DNA Condensation with Polyamines: I. Spectroscopic Studies. *J. Mol. Biol.* **1978**, *121* (3), 311−326.

(58) Chattoraj, D. K.; Gosule, L. C.; Schellman, J. A. DNA Condensation with Polyamines: II. Electron Microscopic Studies. *J. Mol. Biol.* **1978**, *121* (3), 327−337.

(59) Wilson, R. W.; Bloomfield, V. A. Counterion-Induced Condensation of Deoxyribonucleic Acid. A Light-Scattering Study. *Biochemistry* **1979**, *18* (11), 2192−2196.

(60) Todd, B. A.; Parsegian, V. A.; Shirahata, A.; Thomas, T. J.; Rau, D. C. Attractive Forces between Cation Condensed DNA Double Helices. *Biophys. J.* **2008**, *94* (12), 4775−4782.

(61) Ray, J.; Manning, G. S. An Attractive Force between Two Rodlike Polyions Mediated by the Sharing of Condensed Counterions. *Langmuir* **1994**, *10* (7), 2450−2461.

(62) Murthy, V. L.; Rose, G. D. Is Counterion Delocalization Responsible for Collapse in RNA Folding? *Biochemistry* **2000**, *39* (47), 14365−14370.

(63) Tan, Z.-J.; Chen, S.-J. Electrostatic Correlations and Fluctuations for Ion Binding to a Finite Length Polyelectrolyte. *J. Chem. Phys.* **2005**, *122* (4), No. 044903.

(64) Yoo, J.; Aksimentiev, A. Improved Parametrization of Li+, Na+, K+, and Mg2+ Ions for All-Atom Molecular Dynamics Simulations of Nucleic Acid Systems. *J. Phys. Chem. Lett.* **2012**, *3* (1), 45−50.

(65) Pletka, C. C.; Nepravishta, R.; Iwahara, J. Detecting Counterion Dynamics in DNA−Protein Association. *Angew. Chem., Int. Ed.* **2020**, *59* (4), 1465−1468.

(66) Stanley, C.; Rau, D. C. Evidence for Water Structuring Forces between Surfaces. *Curr. Opin. Colloid Interface Sci.* **2011**, *16* (6), 551−556.

(67) Grønbech-Jensen, N.; Mashl, R. J.; Bruinsma, R. F.; Gelbart, W. M. Counterion-Induced Attraction between Rigid Polyelectrolytes. *Phys. Rev. Lett.* **1997**, *78* (12), 2477−2480.

(68) Baker, N. A.; Sept, D.; Joseph, S.; Holst, M. J.; McCammon, J. A. Electrostatics of Nanosystems: Application to Microtubules and the Ribosome. *Proc. Natl. Acad. Sci. U.S.A.* **2001**, *98* (18), 10037−10041.

(69) Jurrus, E.; Engel, D.; Star, K.; Monson, K.; Brandi, J.; Felberg, L. E.; Brookes, D. H.; Wilson, L.; Chen, J.; Liles, K.; Chun, M.; Li, P.; Gohara, D. W.; Dolinsky, T.; Konecny, R.; Koes, D. R.; Nielsen, J. E.; Head-Gordon, T.; Geng, W.; Krasny, R.; Wei, G.-W.; Holst, M. J.; McCammon, J. A.; Baker, N. A. Improvements to the APBS Biomolecular Solvation Software Suite. *Protein Sci.* **2018**, *27* (1), 112−128.

(70) Dolinsky, T. J.; Czodrowski, P.; Li, H.; Nielsen, J. E.; Jensen, J. H.; Klebe, G.; Baker, N. A. PDB2PQR: Expanding and Upgrading Automated Preparation of Biomolecular Structures for Molecular Simulations. *Nucleic Acids Res.* **2007**, *35* (suppl_2), W522−W525.

(71) *The PyMOL Molecular Graphics System*, Version 2.0; Schrödinger, LLC: New York, 2020. pymol.org (accessed September 10, 2020).